Lawrence Berkeley National Laboratory
Recent Work

Title
Investigating the Role of Copper Oxide in Electrochemical CO2 Reduction in Real Time.

Permalink
https://escholarship.org/uc/item/6704782f

Journal
ACS applied materials & interfaces, 10(10)

ISSN
1944-8244

Authors
Mandal, Lily
Yang, Ke R
Motapothula, Mallikarjuna Rao
et al.

Publication Date
2018-03-01

DOI
10.1021/acsami.7b15418

Peer reviewed

Investigating the Role of Copper Oxide in Electrochemical CO_2 Reduction in Real Time

Lily Mandal,[†,‡] Ke R. Yang,[$,Δ] Mallikarjuna Rao Motapothula,[†,‡,Δ] Dan Ren,[†#] Peter Lobaccaro,[†▽] Abhijeet Patra,[‡] Matthew Sherburne,[†&] Victor S. Batista,[$] Boon Siang Yeo,[†#] Joel W Ager,[† &] Jens Martin,*[†§] T. Venkatesan *[†‡§‖€]*

†A Singapore Berkeley Research Initiative for Sustainable Energy, Berkeley Educational Alliance for Research in Singapore, 1 CREATE Way, 138602 Singapore.

‡NUSNNI-Nanocore, National University of Singapore, 117411 Singapore

§Department of Physics, National University of Singapore, 117542 Singapore

‖Department of Electrical and Computer Engineering, National University of Singapore, 117576 Singapore

⊥Centre for Advanced 2D Materials National University of Singapore, 6 Science Drive 2, Singapore 117546, Singapore

#Department of Chemistry, Faculty of Science, National University of Singapore, 3 Science Drive 3, Singapore 117543

▽Department of Chemical and Biomolecular Engineering, University of California, Berkeley, CA 94720 (USA)

&Department of Materials Science and Engineering, University of California Berkeley, CA 94720 (USA)

€Department of Integrative Science and Engineering, National University of Singapore

$ Yale Energy Sciences Institute and Department of Chemistry, Yale University, New Haven, Connecticut 06520-8107, United States

Abstract

Copper oxides have been of considerable interest as electrocatalysts for CO_2 reduction (CO2R) in aqueous electrolytes. However, its role as an active catalyst to reduce the required overpotential and improve the selectivity of reaction compared to polycrystalline copper remains controversial. Here, we introduce the use of selected-ion flow tube mass spectrometry (SIFT-MS), in concert with chronopotentiometry, in-situ Raman spectroscopy and computational modeling, to investigate CO2R on Cu_2O-nanoneedles, Cu_2O-nanocrystals, and Cu_2O-nanoparticles. We show experimentally that the selective formation of C_2 products (i.e. ethylene) in CO2R is preceded by the reduction of the copper oxide (Cu$_2$OR) surface to metallic copper. Based on density functional theory (DFT) modeling, CO2R products are not formed as long as Cu_2O is present at the surface, since Cu$_2$OR is kinetically and energetically more favorable than CO2R.

Introduction

Conversion of carbon dioxide (CO_2), an important greenhouse gas, into energy rich chemicals is a viable approach to reduce the global carbon footprint.[1] Electrochemical CO_2 conversion (CO2R) using renewable electricity is envisaged as a promising technology to achieve this end.[2-7] Among the many catalysts studied for CO2R, copper is unique because it is the only metal that reduces CO_2 to significant amounts of C_2 and higher order hydrocarbons and alcohols.[8,9] Nano-structuring copper into cubes and needles can enhance the selectivity towards C-C coupled products.[10-13] Alternatively, copper oxides can be employed as precursors for making high surface area structures.[14-22] When operated under CO2R conditions (typically -0.8 to -1.1 V vs RHE), the oxides would be reduced to metallic copper (Cu^0) in accordance with the Pourbaix-diagram, producing nanostructured Cu.[23] In the literature, the improved performance of such oxide-derived copper nanostructures towards C_2 products has been attributed to a number of factors: (1) a higher local pH at the catalyst surface favoring the pH-independent C-C coupling pathway over the formation of methane,[13] (2) a higher density of grain boundaries and defect sites optimizing the binding energy of reaction intermediates such as CO,[6,11] and (3) the presence of oxides, subsurface oxygen alongside the metal which provide Cu sites with multiple valences to increase catalytic activity.[14,10]

Studies on copper oxide as a CO2R electrocatalyst showed transient changes in the product distribution attributed to the temporary presence of surface oxide species.[21, 22] Recently, Li et al found that thermally oxidized copper showed stable and improved product generation to CO and HCOOH at lower overpotential compared to polycrystalline copper; however, this performance was not attributed to the oxide itself.[15] This is reasonable given the Pourbaix diagram for Cu,[23]

and was confirmed in their ex-situ XRD study. Kas et al[17] investigated electrodeposited Cu_2O of different orientation and thickness and found that the selectivity depended on the initial oxide thickness and not on the orientation of the starting copper oxide. By performing cyclic voltammetry and employing online electrochemical mass spectrometry (OLEMS), they concluded that CO2R starts only after Cu_2O is reduced into Cu. However, this study did not employ an in-situ characterization of the catalyst surface. Using in-situ Raman spectroscopy, Ren et al. found that in aqueous, CO_2-saturated 0.1 M $KHCO_3$, the surface of a Cu_2O-film reduces within a few minutes to Cu^0 at negative potentials.[14] Interestingly, in this same study it was found that when all signals belonging to copper oxide had disappeared, adsorbed CO, the pertinent reaction intermediate in CO2R, is detected. All these studies suggest that surface Cu^0 and not copper oxide is the active catalyst species.

In contrast, Lee et al.[18] and Mistry et. al.[19] used in-situ X-ray absorption near edge structure (XANES) spectroscopy to show the presence of Cu^+ even after CO2R begins. They proposed that residual Cu^+ is responsible for the improved selectivity to C_2 products found with oxide derived copper. Similarly, Eilert et al,[24] using in-situ ambient pressure XPS, reported the existence of subsurface oxygen during CO2R. They proposed that the enhanced C_2 selectivity is due to subsurface oxygen which changes the electronic structure of the Cu and enhances the binding of CO.

However, they concluded that the catalyst is only present in the Cu^0 state. This contradiction in the results can be explained by the difference in the surface sensitivity of the techniques. XANES is a bulk materials characterization technique in contrast to XPS which is a surface sensitive technique. Mistry et al[19] and Eilert et al[24] both performed further analysis on the sub-

surface of the catalyst utilizing TEM-EDX and TEM-EELS, respectively, with conflicting conclusions. Mistry et al[19] claimed that an oxide phase exists whereas Eilert et al[24] claimed the presence of pure metallic phase with small subsurface oxide.

Summarizing the current literature,[15-20] there are conflicting reports regarding the possible role of copper oxide in CO2R, especially relating to the role of surface copper oxide as the active catalyst. The question remains whether copper oxide itself can be a catalyst[18,19] or if it only acts as the precursor for the formation of nanostructured copper, [14-17] or if it could be leaving behind sub-surface oxygen that influences the copper's activity.[24] Here we investigate whether surface copper oxide itself plays any role as a catalyst for CO2R.

Since copper oxides are quickly reduced under cathodic conditions, and quickly re-oxidized upon the removal of that condition (see SI Fig S18 for details), it is difficult to determine with ex-situ techniques if the periodically measured products are formed on the oxide or on the (largely) metallic surfaces. In-operando, surface sensitive techniques can help to clarify this.[25-26] Previously, real-time product detection and in-operando surface spectroscopy have not been combined to investigate the role of copper oxide. Herein, we combine Raman spectroscopy, with selected-ion flow tube mass spectrometry (SIFT-MS)[27-29] to study in real time both the surface and the products generated during electrochemical CO2R. Density functional theory calculations were employed to model the system, and could rationalize the results very successfully.

SIFT-MS can detect and quantify gaseous products such as methane, ethane, and ethylene as well as higher order hydrocarbons, like propene, in a time scale of 0.1 to 10sec (depending on the number of masses scanned). This enables the capture of reaction dynamics. In this way, it overcomes the classic problem faced in much of the literature where the gaseous products of CO2R are analyzed by gas chromatography (GC) with analysis times in the range of minutes. In

addition, liquid products, typically detected by high pressure liquid chromatography (HPLC) or nuclear magnetic resonance spectroscopy (NMR), are only measured once at the end of an experiment by sampling aliquots of the electrolyte.[9,20,25,26,30] SIFT-MS allows the simultaneous detection of liquid products with finite vapor pressure - this aspect of the technique will be presented in another paper. SIFT-MS is able to provide this real-time analysis of complex multi-component mixtures due to its use of gentle chemical ionization reactions. These reactions, such as proton addition, avoid the fragmentation of molecules typical of electron ionization MS which result in an extremely low limits of detection (LOD) of the parent ion.[26] SIFT-MS has been well reviewed in the literature and we point the reader to these works [27-29]for a deeper understanding of the advantages of this technique. We have published technical details of SIFT-MS applied to CO2R elsewhere [30]

Here, three different forms of Cu_2O were synthesized by electrochemical and thermal methods [14, 15, 31] yielding oxide-derived catalysts of different surface structures and different CO2R activities. These catalysts were subsequently evaluated in real-time, using an electrochemical cell previously detailed,[32] to determine the onset of CO2R after switching on a constant cathodic current. By combining DFT study and in-situ Raman with real time product detection, we show that Cu_2O reduction (Cu_2OR) typically occurs before CO2R begins since Cu_2OR is energetically more favorable. Interestingly, Cu_2O with certain exposed surfaces could be active catalysts for CO2R if were not poisoned by reaction intermediates.

2. Experimental Section

Detailed experimental procedures are in the Supporting Information.

2.1 Preparation of catalyst.

Three types of copper oxide were prepared for this study. The first was synthesized by thermally annealing copper foils in a tube furnace at 450 ºC for 3 hrs (Cu NPs).[15] Copper oxide nanocrystals (Cu NCs) were synthesized by a method previously reported.[14] Copper oxide nanoneedles (Cu NN) were synthesized by anodizing the Cu foil in 2M KOH solution in a two electrode setup using graphite as counter electrode. The electrode anodization was carried out at a constant current density of 7 mA/cm^2 for 5 mins for synthesizing $Cu(OH)_2$, after which it was annealed in vacuum at 700 ºC to convert the $Cu(OH)_2$ into Cu_2O nanoneedles.[31]

2.2 In situ Raman spectroscopy. In situ Raman spectroscopy was carried out with a confocal Raman microscope (Modular system from Horiba Jobin Yvon) in an epi-illumination mode (top-down). A He-Ne laser with 633nm wavelength (CVI Melles Griot) was used as excitation source. A water immersion objective lens (LUMFL, Olympus, 60x, numerical aperture: 1.10) covered with a 0.013 mm thin Teflon film (American Durafilm) was used to focus and collect the incident and scattered laser light. The back-scattered light was filtered through a 633 nm edge filter, before being directed into a spectrograph (iHR320) / charge-coupled device detector (Synapse CCD). The electrochemical Raman cell was a round Teflon dish with the detachable Cu electrode mounted in the middle.[51] The acquisition time for each spectrum was 10 sec.

2.3 Computational Details:

We used the Vienna ab initio simulation package (VASP)[33-36] for all periodic boundary calculations. Projector augmented plane wave (PAW)[37,38] method together with the PBE exchange-correlation functional[39] were employed to describe the electron-ion interactions. A cutoff of 450 eV was chosen for the plane wave basis set in all calculations. A $5 \times 5 \times 5$ Monckhorst-Pack type k-point grid was chosen for the optimization of bulk Cu and Cu_2O. The

Gaussian smear method was used for Cu_2O and Cu. The σ value was chosen to be 0.1 eV for both cases. The energy convergence criterion was set to be 10^{-6} eV per unit cell and the force convergence criterion of 0.03 eV $Å^{-1}$ was used for all structure optimization. <mark>We noted that sometimes the geometry optimization converges to stationary structures rather than energy minimum structures (Figure S7). Therefore we optimized all intermediates structures without symmetry constraints and always did frequency calculations to confirm the optimized structures are energy minimum structures.</mark> For the calculation of transition states (TSs), a tighter convergence criterion of 10^{-8} eV per unit cell was used. We used nudged elastic band (NEB) method[40] to locate the proper guess TS geometries, which were then optimized to saddle points with improved dimer method [41]. Frequency calculations were performed to confirm the nature of located transition states. A $3 \times 3 \times 1$ Monckhorst-Pack type k-point grid was chosen for slab calculations. Slab models were chosen to have 4 unit cells, which corresponds a coverage of $\theta = $ ¼. Seven layers of Cu were used to construct the Cu(111) slab model, while six atomic layers (3 layers of Cu and 3 layers of O) were used to construct the $Cu_2O(111)$ and $Cu_2O(200)$ slab models. The sizes of slab modes were chosen to be 5.13 Å × 5.13 Å × 33.86 Å, 6.084 Å × 6.084 Å × 22.452 Å and 6.084 Å × 6.084 Å × 23.605 Å for the Cu (111), $Cu_2O(111)$ and Cu_2O (200) surfaces. During the geometry optimization of the slab models, bottom five layers of Cu(111) slabs and bottom two layers (one layer of Cu and one layer of O) of $Cu_2O(111)$ and Cu_2O (200) slabs were fixed at the bulk position.

The relative energies of intermediates of CO_2 reduction (CO_2R), and hydrogen evolution reaction (HER) as well as Cu_2O reduction (Cu_2OR) were calculated relative to CO_2, H_2, and bare surfaces. For reactions involving the release of H_2O, e.g. *COOH to *CO, the energy of isolated H_2O was used in the calculations. A supercell of 15.0 Å × 15.0 Å × 15.0 Å, the Gaussian smearing method

and a σ value of 0.1 eV were used in the calculations of small molecules. For reaction steps involving the H^+ and e^-, the computational hydrogen electrode (CHE) technique developed by Nørskov *et al*. [42] was used to consider the dependence of relative energies on pH and applied bias potential and the detailed calculation approach is shown in Scheme S1(see computational detail in SI). The dispersion interactions were considered with Grimme's D3 correction[43] and the solvation effects were considered with implicit solvation model as implemented in VASPsol. [44] A dielectric constant of 80.0 was used to represent bulk water solvent. The effects of dispersion and solvation are shown in Figure S9-S11. Frequency analysis was performed for both absorbates and surfaces atoms which are allowed to relax to calculate thermal correction to the free energies which are listed in Table S4-S7. Please refer the supporting information for more computational details.

3. Results and Discussion

3.1 Characterization of electrocatalysts. Scanning electron microscopy (SEM) images of catalyst precursor structures formed from nano-needles (NNs), cubic nanocrystals (NCs), and nanoparticles (NPs) before and after CO2RR are shown in Figures 1a-f. Clearly, the morphology of all catalysts after reduction is different, and different from the pristine Cu_2O state (also distinct from planer electropolished Cu Figure S2). In particular, we note that the reduced catalysts appeared to be composed of small particles which could increase the effective catalytic area and provide a variety of defects and step-edges sites. Figure 2a, c and e shows the XRD patterns of the copper oxide samples before and after CO2R. In all samples before CO2R, we can identify peaks corresponding to Cu_2O and the underlying Cu substrate in accordance with database patterns extracted from the International Center for Diffraction Data (ICDD No-01-077-0199 for Cu_2O and 00-004-0836 for Cu). The Cu_2O samples have different preferential orientations,

shown by the higher intensities of (200) peak of NCs versus (111) peak of NPs. Interestingly, all three catalysts showed different preferential orientations after reduction as well; NCs and NNs showed higher intensities of Cu (200) peak versus Cu (111) peak of NPs.

The Raman spectra collected under ambient conditions before and after CO2R are shown in Figure 2b, d, f and the identified Raman peaks are listed in Table S1. Interestingly, NNs and NPs samples show Cu_2O peaks slightly below Γ_{12}^- at 109 cm^{-1} and $\Gamma_{15}^{(1)}$ at 154 cm^{-1} (LO) possibly due to defect formation or strain. In contrast, the NC sample shows Cu_2O peaks close to the expected values and with low Raman intensity. In perfect crystals, Γ_{12}^- and $\Gamma_{15}^{(1)}$ phonon modes are IR active and Raman inactive.[45]

In the following sections, we investigate the initial period of Cu-oxide reduction in more detail employing in-situ spectroscopic methods and DFT-modeling.
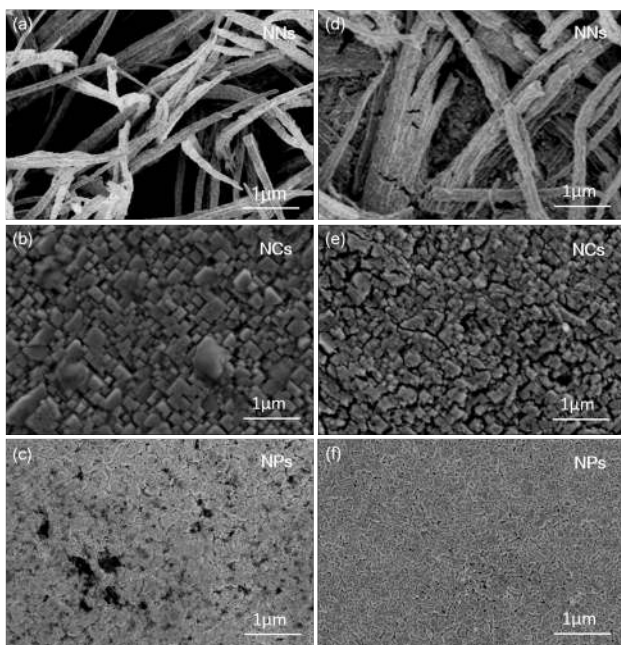
Figure 1. SEM images (scale 1μm) of as prepared copper oxides before CO2RR (a) nano-needles (NNs), (b) nano-crystals (NCs), and (c) nano-particles (NPs) after CO2RR (d) nano-needles (NNs), (e) nano-crystals (NCs), and (f) nano-particles (NPs)
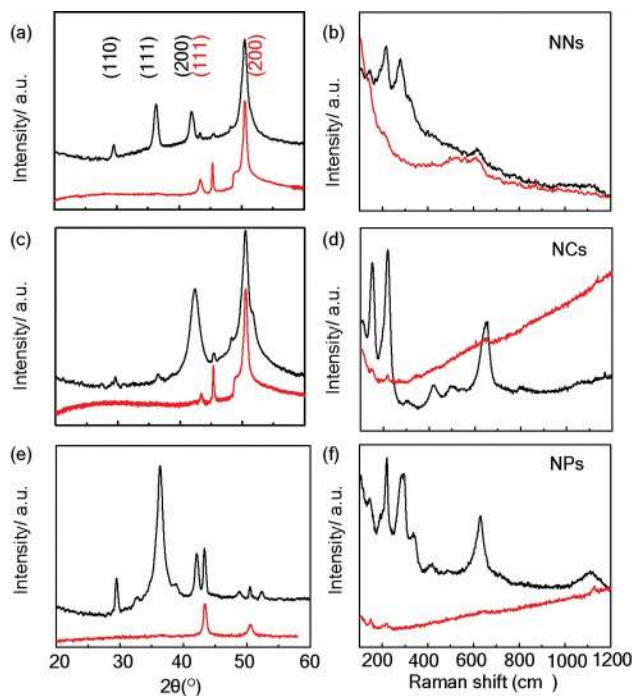

Figure 2 XRD pattern of copper oxide before (black) and after CO2R (red)(a) NNs, (c) NCs and (e) NPs showing peaks corresponding to Cu_2O (black) and underlying Cu substrate (red). (e) Raman spectra of copper oxide before (black) and after CO2R (red) (b) NNs, (d) NCs and (f) NPs showing peaks corresponding to Cu_2O (109, 152, 415, 645), CuO (303, 634) and $Cu(OH)_2$ (490)

3.2 In-situ measurement of CO2R products.

A benchmark study was performed to validate that the CO2R production measurements made by SIFT-MS agree with those performed with traditional techniques such as GC (see Figure S1 for experimental setup). The products from copper oxide NNs operated at a constant current

density of -10 mA/cm^2 were measured. Figure 3a shows the GC data and overlaid SIFT-MS data

for methane, ethylene, and propene (SIFT-MS detects all hydrocarbons but cannot detect H$_2$ and

CO). The extracted FEs of both methods coincided within experimental uncertainties. Additional

comparative data for SIFT and GC are provided in the SI (Figure S4). Figure 3b shows the real-

time measurement of FEs for methane (C$_1$), ethylene (C$_2$), and propene (C$_3$). As explained

below, during the first few minutes Cu$_2$O reduction predominates and we do not observe CO2R

product in SIFT-MS. The sensitivity of the SIFT-MS technique is evident from the detection of

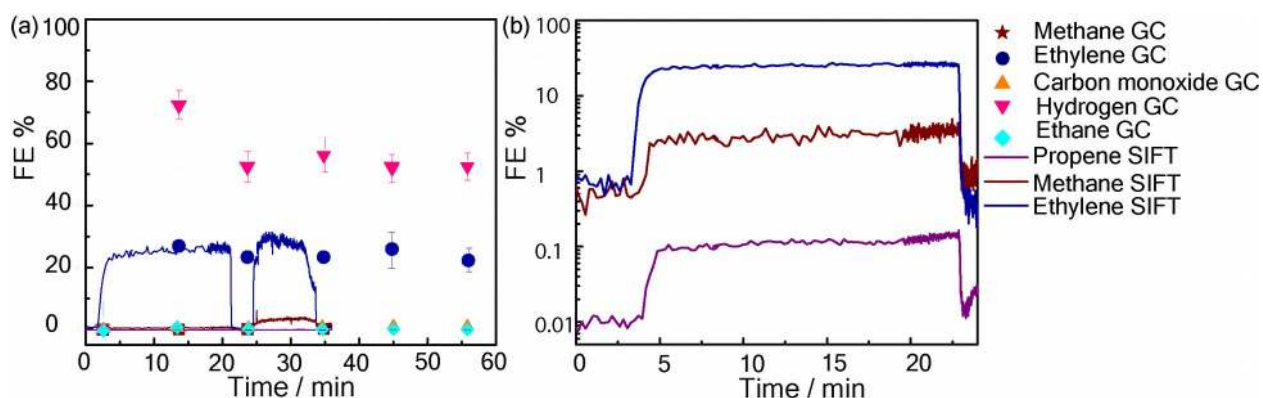the C$_3$ product with only 0.1% FE. Detailed FEs of the products are listed in SI (Table S2).

Figure 3. (a) Comparison of GC (points) and SIFT-MS data (lines) from Cu NNs operated at

-10mA/cm^2 in 0.1M KHCO$_3$. (b) Semi-log plot of SIFT-data for methane (C$_1$), ethylene (C$_2$), and

propene (C$_3$).

Once a current is applied to a Cu$_2$O cathode, three reduction processes are possible, namely:

CO2R, hydrogen evolution reaction (HER), and Cu$_2$OR to metallic copper. In order to identify

the dominant reaction in the initial phase we take advantage of the real time sensitivity of SIFT-

MS. Figure 4 shows the chronopotentiometry (CP) and online SIFT-MS data of the different

samples (the liquid products are shown in Figure S5). In a CP measurement constant current is

applied to an electrochemical cell and the change in voltage is measured as a function of time. Different current densities are chosen for different samples such that the long-term potential for all samples is approximately -0.8 V versus the reversible hydrogen electrode (RHE), a good operational condition for CO2R.[14, 15] The CP curve for all samples possesses a slightly negative initial potential $V_i \approx$ -0.2V vs. RHE up to a time (t_i) when the potential steeply increases to stabilize at a final potential $V_f \approx$ -0.8 V. The observed change in potential from V_i to V_f is due to change in the surface reaction at the cathode from copper oxide reduction during V_i, t_i to CO2R after that and explained in detail in SI-V. Time traces for NCs samples run at different current densities are shown in the SI (Figure S6). In all cases, CO2R products are detected only after the increase in the overpotential measured in CP. This provides strong evidence that at the beginning, Cu_2OR is kinetically favored relative to CO2R. Only when Cu-oxide is essentially completely reduced to metal does CO2R begin.
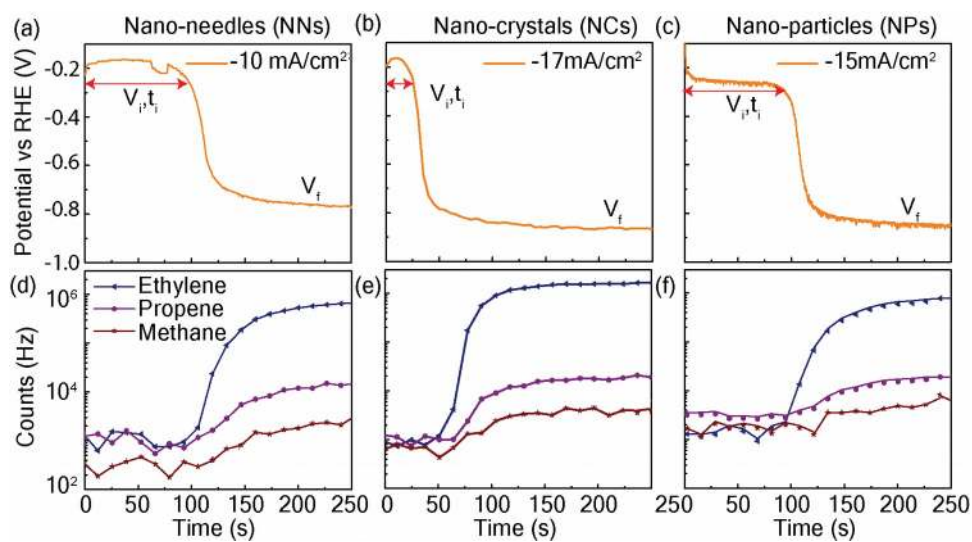

Figure 4. CP (top) and SIFT-MS data (bottom) of Cu_2O a), d)NNs driven at -10mA/cm^2 b), e)NCs driven at -17 mA/cm^2 and c), f) NPs driven at -15 mA/cm^2, all in 0.1 M KHCO$_3$

13

electrolyte saturated with 1 atm CO_2. The SIFT-MS data is corrected for its intrinsic response time (see SI-III, Figure S3).

Since SIFT-MS cannot detect CO and H_2, we have conducted GC measurements to rule out HER during the initial phase. Due to the slow time evolution of GC we slowed down the rate of Cu_2O reduction to stretch the initial phase t_i. Hence, we have run the samples at very low constant current density of -1 mA/cm^2. Figure 5 shows the chronopotentiometry and GC data of NCs and NNs under such conditions confirming that there is no HER and no CO2R products (including CO and H_2) during the initial period t_i. Cu NPs run at -1 mA/cm^2 did not fully reduce during the 1 hr reaction and no products are observed by GC shown in the SI (Figure S7).
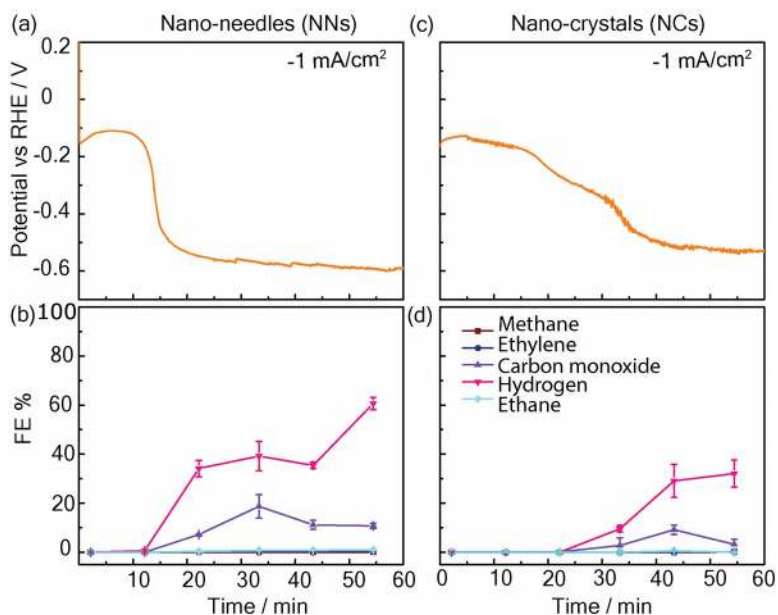

Figure 5. Evolution of CO and H_2 at low current density. a) NC Chronopotentiometry b) NN Chronopotentiometry c) NC GC data, d) NN GC application of current, GC data shows only negligible amount data evolution of CO and H_2 during the first 10-20 mins where Cu_2OR prevails in 0.1 M $KHCO_3$ electrolyte saturated with 1 atm CO_2.

3.3 Density Functional Theory Modeling. To rationalize the distinct reactivity of Cu_2O NCs, NNs, and NPs, we analyzed the reaction free energy profiles of CO2R at the density functional theory (DFT) level, using the Vienna ab initio simulation package.[33-36] Figure 2 shows that the dominant XRD peak of Cu_2O NPs corresponds to the (111) surface, while for Cu_2O NCs corresponds to the (200) surface, while Cu_2O NNs exhibit both (111) and (200) surfaces. Therefore, we calculated the relative free energies of intermediates of CO2R, and HER, as well as Cu_2OR, on both Cu_2O (111) and Cu_2O (200) relative to CO_2, H_2, and bare surfaces. In addition, we computed the relative free energies of intermediates of HER and CO2R on Cu (111).

Figure 6a shows the DFT optimized geometries of model surfaces of Cu (111), Cu_2O (111) and Cu_2O (200). The Cu-Cu distance on Cu (111) is 2.57 Å, similar to that of bulk Cu. In contrast, the Cu atoms on Cu_2O (111) and Cu_2O (200) are significantly spaced more due to their coordination to O atoms (Figure S8). In addition, the presence of sub-surface O atoms create different binding sites leading to different binding modes and reactivity of molecular adsorbates. For example, with the PBE functional, CO prefers to bind at FCC sites on the Cu (111) surface, with a binding energy of -0.79 eV, consistent with previous studies.[47] However, as shown in Figure S8, on the Cu_2O (111) surface CO prefers to bind at the atop position of Cu atoms (-1.37 eV) and on the Cu_2O (200) surface CO binds at the bridge site (-1.34 eV) forming stronger bonds than on Cu (111).

We first analyze the HER and CO2R on Cu (111). Figure 6b shows the relative free energies of intermediates of HER and CO2R. The reduction of protons to form surface-bound hydrogen atoms is energetically favorable, and the subsequent reduction to release H_2 requires only 0.12 eV, consistent with the experimental observation that hydrogen is the major product at low bias

potentials.[48] The reduction of CO_2 to CO needs to overcome the high energy intermediate

*COOH with a relative free energy of 0.52 eV, while further reduction of CO needs to overcome

the high energy intermediate *CHO with an energy increase of 0.76 eV. Both energy uphill steps

involve redox processes which can thus be driven by applying a potential. As shown in Figures

SI-12, the total energy balance for CO reduction products becomes negative when applying a

bias potential more negative than -0.76 eV, respectively, yielding estimated onset potentials

consistent with previous experiments [48] and computations.[49]

Next, we analyze the reduction of Cu_2O surfaces through Cu_2OR and CO2R reaction pathways.

Figures 6c and 6d show the relative free energies of the intermediates of HER, CO2R, and

Cu_2OR on Cu_2O (111) and Cu_2O (200). As mentioned above, CO binds more strongly on Cu_2O

surfaces than on Cu (111). In addition, all other intermediates of CO_2 reduction are more

stabilized on Cu_2O surfaces. Furthermore, the reduction of a proton to form surface-bound

hydrogen is energetically very favorable on Cu_2O (111), more favorable than CO2R pathways.

However, the reduction of the second proton to release H_2 requires an energy increase of 0.66 eV.

The reduction of subsurface O atom to form surface bound OH on Cu_2O (111) is energetically

very favorable but the further reduction of surface bound OH to H_2O is slightly energy uphill.

With bias potentials more negative than -0.07 V, it is possible to open a Cu_2OR pathway to

reduce surface-bound hydroxyl groups to H_2O (Figure S13a). At even more negative bias

potential (< -0.78 V), the reduction of surface-bound CO is also possible, leading to hydrocarbon

products (Figure S13 c). Similar energetics apply to Cu_2O (200) (Figure S14). Again, the

reduction of subsurface O atoms to form surface-bound hydroxyl groups, and ultimately H_2O, is

very favorable. We note that the binding location for H and OH differ (Figure SI-8) and

consequently, the strong binding energy of H does not hinder Cu_2OR. Thus, Cu_2OR on Cu_2O

(200) is more favorable than the HER or CO2R and it is the expected reaction to proceed (for energy diagrams under bias see Figure S14). We note that the reduction of surface-bound CO on Cu$_2$O (200) requires much less energy than on Cu(111), suggesting CO2R on Cu$_2$O(200) is possible. However, the Cu$_2$OR is energetically favorable and expected to be the dominant reaction. For completeness, we also highlight that a surface oxygen atom is easily removed from Cu surfaces (Figure S15).

The calculated energetics suggest Cu$_2$OR is thermodynamically more favorable than CO2R on both Cu$_2$O(111) and Cu$_2$O(200). We also located transition states associated with Cu$_2$OR and CO2R on both surfaces and the results are given in Figure S16. The barriers for Cu$_2$OR are much lower than those for CO2R. Therefore, Cu$_2$OR is both energetically and kinetically more favorable than CO$_2$R on both copper oxide surfaces.
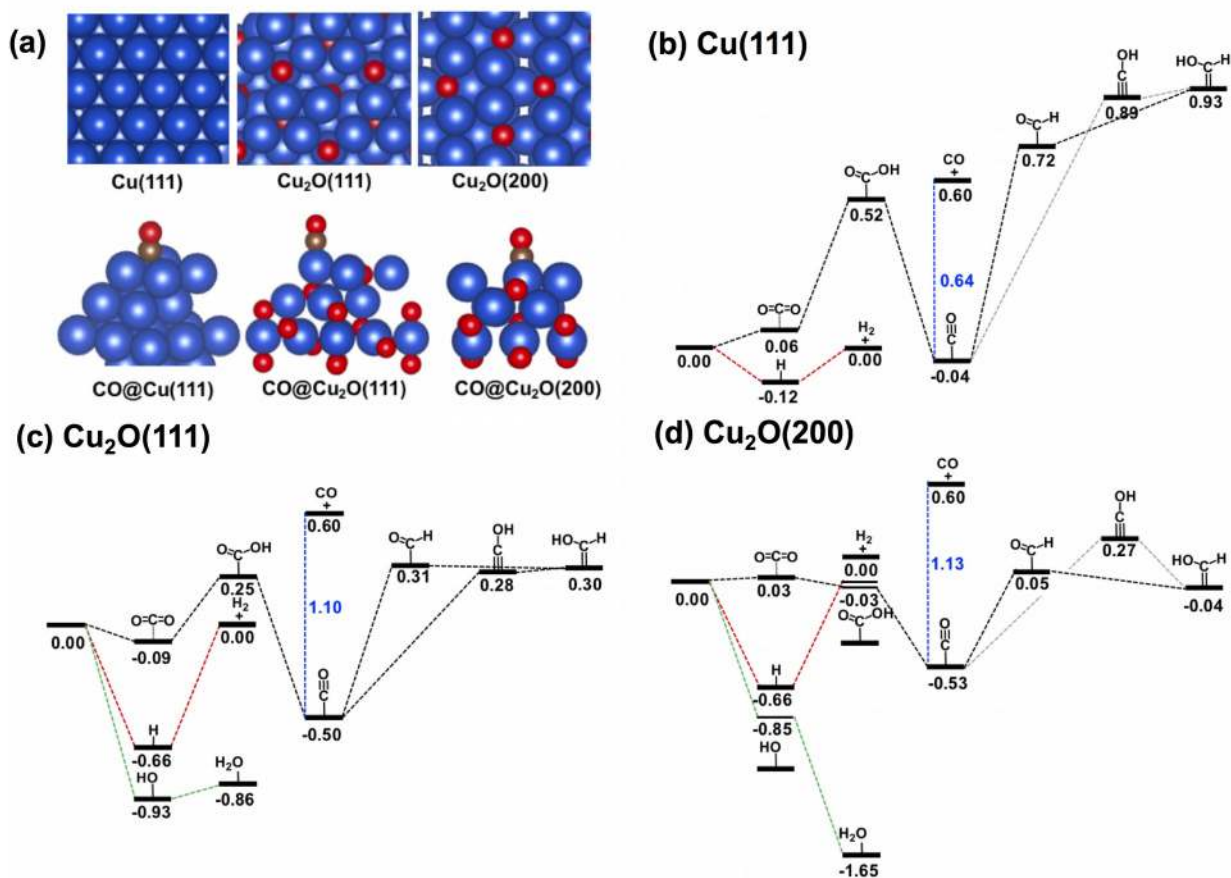
Figure 6. DFT optimized geometries and relative free energies of intermediates of HER (red dash line), CO2R (black dash line), and Cu_2OR (green dash line) on Cu (111), Cu_2O (111), and Cu_2O (200) relative to CO_2, H_2, and bare surfaces. a) DFT optimized surfaces of Cu(111), Cu_2O(111), and Cu_2O (200) and CO absorption geometries at the fcc site of Cu (111), Cu atop site of Cu_2O (111), and bridge site of Cu_2O (200); Calculated binding free energies of intermediates on b) Cu(111), c) Cu_2O(111) and d) Cu_2O(200) surfaces [in eV].

3.4 In-situ **Raman spectroscopy.** We now discuss in-situ Raman spectra for the different copper oxide samples. Figure 7b shows the time dependent Raman spectra of NCs (the corresponding CP curves are shown in Figure S17). The black curve was taken as reference and is measured in the original condition before the reaction has started (no current is applied). We can identify peaks at 144, 215, 528 and 623 cm^{-1} corresponding to Cu_2O.[50] After application of current, the next Raman spectrum is taken at 10 s and shows a significant enhancement in intensity. The signal enhancement can be either due to surface enhanced Raman Spectroscopy (SERS) [51]or inelastic light scattering by charge carrier-excitations in the metal (i.e. by electron-hole pair excitations) which are made possible by the breakdown in momentum conservation caused by the sub-microscopic surface roughness.[52] Considering that enhancement in Raman spectra (RS), is observed we conclude that a metal Cu layer forms as Cu_2O reduction starts while residual oxide remains present in the bulk. With enhancement in RS, there is a corresponding change in background signal making it hard to interpret the peaks in the range of 100 - 250 cm^{-1}. Hence, we focus on Cu_2O peaks between 250 and 750 cm^{-1}. After the current is applied the Raman peaks attributed to Cu_2O (528 and 623 cm^{-1}) show a sudden decrease in the intensity. Further, there are indications of Cu defect related peaks in the region of (100-250 cm^{-1}).[51] These observations are consistent with an immediate formation of a metallic Cu surface layer once current is applied. The limits of detection of our Raman spectroscopy measurements do not allow us to determine if there could be trace amounts of residual O atoms embedded in the catalysts.
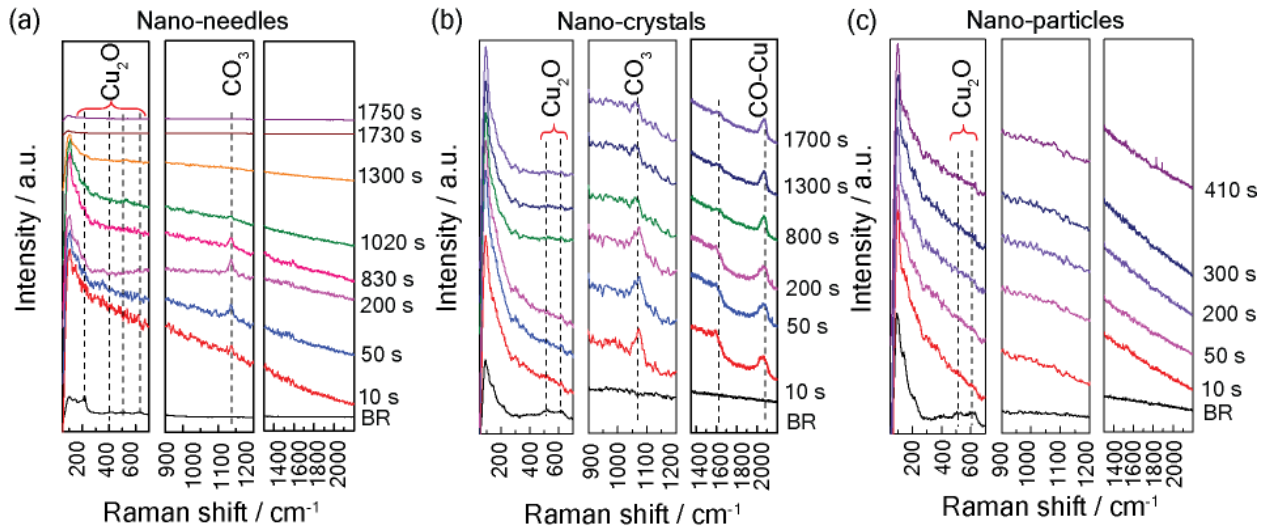
Figure 7. In operando Raman spectroscopy runs at 10s integration each with a constant current density of -1 mA/cm^2 in CO_2 saturated 0.1M KHCO$_3$ solution for (a) Cu$_2$O nanoneedles, (b) Cu$_2$O nanocrystals and (c) Cu$_2$O nanoparticles. Each Raman spectrum is divided into 3 parts to display the Cu$_2$O, carbonate, and Cu-CO Raman bands.

The Raman spectra provide additional information on CO2R reaction intermediates. Figure 7b shows the instantaneous appearance of new peaks at 1074 and 2060 cm^{-1} after the application of current. The 1074 cm^{-1} peak is attributed to the stretching mode of adsorbed CO_3^{2-} (CO$_{3ad}$)[53,54] (the bicarbonate deprotonates after adsorption) consistent with observation of Xu et al.[55,56], Hori et al.[57] and Wuttig et.al.[58]. The adsorbed carbonate is surface absorbed species and do not participate in the CO2R. When electrochemical CO2R is performed in Ar purged bicarbonate solution no CO2R products are generated; thus, there is no possibility of electroreduction of bicarbonate (i.e. bicarbonate as active species in CO2R). In a recent report, Dunwell et al.[55] used in situ spectroscopy and isotopic labeling to show that bicarbonate increases the reducible CO_2 concentration (dissolved CO_2) in the solution through rapid equilibrium exchange between

aqueous CO_2 and bicarbonate near the electrode surface. For Cu NCs samples we see the decrease in the concentration of CO_3^{2-} near the surface with time. This can be assigned to the increase in potential (see Figure S6a), as higher negative electrode potentials decrease the adsorption of anions. The peak at 2060 cm^{-1} is attributed to adsorbed CO.[58-61] While Raman spectra shows the appearance of CO on NCs within seconds after the application of current, the corresponding GC data shows only negligible production of CO, H_2, or any other hydrocarbons during the first twenty minutes (Figure 5a, b). The applied current density of -1 mA/cm^2 corresponds to a very low potential which cannot reduce CO further. However, for Cu_2O NCs, with dominant (200) surfaces exposed, Cu_2OR can occur at very low potential as shown by our DFT calculation. Hori et. al.[61] have shown that adsorbed CO suppresses hydrogen generation and other electrochemical reductions. Indeed, the rate determining step in CO2R is the step following CO adsorption. [59-62]Thermodynamic analysis shows that high coverage of CO blocks hydrogen absorption sites inhibiting C-H bond formation. [63,64] Our DFT calculations show that Cu_2OR is energetically the most favorable reaction pathway, but with the Cu-site blocked by CO, CO2R and HER have also a dynamic disadvantage. Consequently, Cu_2OR will dominate until almost all the oxide is reduced.

Figures 7a and c show the Raman spectra of NNs and NPs, respectively. Consistent with our observations on NCs we find quasi instantaneous reduction of copper oxide related peaks within the first few seconds, confirming the formation of copper. Interestingly, the three copper oxide samples differ in terms of the bicarbonate and adsorbed CO peaks. Compared to NCs, the NNs show a very weak CO peak, whereas NPs do not show any adsorbed CO peaks. As shown in Figure 1, all the three catalysts on reduction generates different nanostructures with different

defect densities and preferential crystal orientations, as shown by the higher intensities of (200) peak of NCs versus (111) peak of NPs. Consequently, under-coordinated sites, such as defects and boundaries, are expected to be different in all three catalysts. The difference in the intensities of the CO peak can be related to the adsorption strength of CO on these different defects and crystal orientation. This is also evident by the difference in product distribution on the three catalysts shown in Table S2. A direct quantitative comparison of the selectivity and efficiency of these SERS-active Cu films (Cu NC, Cu NN and Cu NP) relative to each other is not possible as the SERS intensity is convoluted with the different surface structures of the reduced Cu. We nonetheless observe that Cu NC and Cu NN samples are capable of producing higher order C2-C3 products such as propylene (detected by SIFT-MS) and propanol (detected by head space GC) compare to Cu NP sample (see table S2 and S3). This is consistent with the more intense absorbed CO peak in the Raman spectra shown in Figure 7a and b. For Cu NC sample we observed the inhibition of the catalyst surface to liberate the electro-generated CO. This indicates that there could be a high population of surface adsorbed CO which is necessary for conversion to higher order products.[57]

To empirically validate the claim that essentially all Cu_2O is reduced within the initial time t_i, we estimate the effective thickness of reduced Cu_2O based on the partial current density for Cu_2O reduction. Based on our experimental findings, we assume that all current goes to Cu_2O reduction until CO2R or HER products are detected. Afterwards, the measured CO2R and HER contributions are subtracted from the total current to find the current still going towards Cu_2O reduction. For this estimate, we use NCs because of their simplified morphology (Figure 1b, Figure SI 19a). Figure 3c shows that within the first 54 seconds there is no change in the SIFT

background signal, thus all applied current is assumed to be consumed by Cu_2OR. The calculated thickness of the reduced Cu_2O layer is 1.1 ± 0.1 µm which is consistent with the estimated thickness of Cu_2O in the NC samples of 1.2 ± 0.1 µm as determined by cross-sectional SEM (Figure SI-19(a)).

In a second estimation, we use data from the much lower current density experiments (Figure 4 a, b). Within the initial time (t_i = 700s), an estimated 860 nm of Cu_2O is reduced which is less than the estimated total thickness of the Cu_2O layer from SEM images. However, we note that the Cu_2O peaks disappear from the Raman spectra within 10 seconds of applying a potential, thus the reduction must proceed from the surface deeper into the bulk of the catalyst. Therefore, the residual copper oxide yet to be reduced must be present in the bulk of the catalyst. This leaves open the possibility that Cu_2O reduction continues at a lower rate in the bulk in parallel to CO2R and HER at the surface once the potential has increased (Figure SI 20). With this assumption, we calculate that all of the Cu_2O is completely reduced to Cu within 20 mins, similar to the observations by Lee et al and Mistry et al. A similar calculation for Cu NP sample is given in SI-X.

Oxide derived Cu nanostructures can easily re-oxidize under OCP condition as shown in Fig S17 and Lum et al [46] compromising the ex situ measurement. From the reduction of Cu_2O-peaks and the apparent noise level in the after CO2R XRD-spectra, we can estimate an upper bound of residual crystalline Cu_2O of 3%. By comparing the heights of residual Cu_2O related peaks in Raman spectra, we can estimate an upper bound of 6% of Cu_2O. In contrast to XRD which measures the bulk, Raman spectroscopy is more surface sensitive which explains the larger estimate for residual Cu_2O. Considering a typical thickness of 4nm of natural Cu_2O, we conclude that residual Cu_2O is not more than 6%, consistent with recent studies.[46]

The high C2(ethylene)/C3(propane, propanol) product selectivity exhibited by these catalysts is due the higher defect density in these catalysts supporting adsorption of CO as shown by Ren et. al.[14] and Li et. al.[15] ==Further~~more~~, the OD Cu have high ~~geometrical~~ surface area~~s~~ (because of the nanostructure) leading to high local current density. During CO2R and HER, protons from water are consumed and OH- ions are released at the electrode surface; increasing the local pH near the electrode surface. The high local pH favors C-C coupling at low overpotential versus RHE as shown by Koper et. al.[64] and Lum et. al. [67] The high local pH on the catalyst surface favours the CO dimerization pathway for ethylene formation==. It should be noted that in-situ SIFT-MS and the limits of detection of our Raman spectroscopy measurements do not allow us to determine if there could be trace amounts of residual O atoms embedded in the catalysts, as reported earlier by Nilsson et al.[24,65] and Favaro et. al.[68] We highlight here though that copper oxides are extremely prone to be reduced to Cu metal at the potentials used in this work.[23] Hence, we believe that if there is any residual O, it should be in the bulk rather than on the surface.

4. Conclusions.

In summary, by operando SIFT-MS, computational modeling and Raman spectroscopy, we show that in three oxide-derived Cu electrocatalysts, with differing surface morphologies and crystal orientation, surface copper oxide reduces prior to CO2R. Even Cu_2O (200) seems to be a possible catalysts for CO2R based on our DFT modeling, CO2R products are not formed as long as Cu_2O is present at the surface, since Cu_2OR is kinetically and energetically more favorable than CO2R. While, we cannot exclude a small percentage of residual oxygen, it is unlikely that it will be present in the form of Cu_2O. We note, that the existence of O near the surface has been claimed in [ref].Looking forward, the exceptional performance of SIFT-MS for real time

electrochemical CO2R can offer new applications in time-resolved monitoring of reaction intermediates and liquid product detection.

ASSOCIATED CONTENT

Supporting Information.

Experimental Procedures; Computational Details; schematic of the whole setup; Dead time of the SIFT-MS; Chronopotentiometry in- operando SIFT-MS data on electropolished Cu ;SEM images of electropolished Cu before and after CO2R; Raman peaks of copper oxide samples; Comparative data for SIFT and GC for polycrystalline copper; Cu_2O NNs, NCs and NPs; FE of product measured using GC, head space GC and HPLC; Cu_2O NCs run in SIFT-MS at different current density; FE of CO2R products measured using GC, head space GC and HPLC for nano-needles and nano-crystal run at -1mA/cm^2;chronopotentiometry and GC data of Cu_2O NPs run at -1mA/cm^2; Binding geometries and energies of H, CO, and H-O$_{Cu2O}$ on Cu_2O surfaces; Binding energies of intermediates on Cu and Cu_2O surfaces; Thermal corrections of intermediates; Relative free energies at different bias potentials; Free energy to remove O atom on Cu(111); Geometries of transition states for Cu_2OR and CO_2R on Cu_2O surfaces and associated barrier height; Chronopotentiometry curve for in-operando Raman spectroscopy; In-situ Raman spectra of Cu NCs; Cross sectional SEM image of Cu_2O NCs; Thickness calculation Cu_2O NCs; Coordinates of all intermediates in VASP format

AUTHOR INFORMATION

Corresponding Authors

* T. Venkatesan, E-mail: venky@nus.edu.sg phone: (65) 6516 5187

 * Jens Martin, E-mail: phyjm@nus.edu.sg phone: (65) 6516 4140

 *Joel W Ager, E-mail: jwager@berkeley.edu phone:

Author Contributions

The manuscript was written through contributions of all authors. All authors have given approval to the final version of the manuscript. KRY and MM contributed equally.

 ABBREVIATIONS

CO2R   carbon dioxide reduction

Cu_2OR copper oxide reduction

CP   chronopotentiometry

GC   gas chromatography

SIFT-MS   soft ionization flow tune mass spectrometry

HER   hydrogen evolution reaction

FE   Faradaic Efficiency

References

1) Graves, C.; Ebbesen, S. D.; Mogensen, M.; Lackner, K. S. Sustainable hydrocarbon fuels by

recycling CO_2 and H_2O with renewable or nuclear energy. *Renew. Sustain. Energy Rev.* **2011**, *15*,

1–23.

(2) Zhu, D. D.; Liu, J. L.; Qiao, S. Z. Recent Advances in Inorganic Heterogeneous

Electrocatalysts for Reduction of Carbon Dioxide. *Adv. Mater.* **2016**, *28*, 3423–3452.

(3) Kumar, B.; Brian, J. P.; Atla, V.; Kumari, S.; Bertram, K. A. ; White, R. T. ; Spurgeon, J. M. New trends in the development of heterogeneous catalysts for electrochemical CO_2 reduction. *Catal. Today* **2016**, *270*, 19–30.

(4) Lu, Q., Rosen, J.; Jiao, F. Nanostructured Metallic Electrocatalysts for Carbon Dioxide Reduction. *Chem. Cat. Chem.* **2015**, *7*, 38–47.

(5) Jones, J.-P.; Prakash, G. K. S.; Olah, G. A. Electrochemical CO_2 Reduction: Recent Advances and Current Trends. *Isr. J. Chem*. **2014**, *54*, 1451–1466.

(6) Qiao, J.; Liu, Y.; Hong, F.; Zhang, J. A review of catalysts for the electroreduction of carbon dioxide to produce low-carbon fuels. *Chem. Soc. Rev.* **2014**, *43*, 631–675.

(7) Costentin, C.; Robert, M.; Savéant, J.-M. Catalysis of the electrochemical reduction of carbon dioxide. *Chem. Soc. Rev*. **2013**, *42*, 2423–2436.

(8) Y. Hori in Modern Aspects of Electrochemistry, Vol. 42 (Eds: C. G. Vayenas, R. E. White, M. E. Gamboa-Aldeco) *Springer*, New York, **2008**, 89-189.

(9) Kuhl, K. P.; Cave, E. R.; Abram, D. N.; Jaramillo, T. F. New insights into the electrochemical reduction of carbon dioxide on metallic copper surfaces. *Energy Environ. Sci.* **2012**, *5*, 7050–7059.

(10) Reske, R.; Mistry, H.; Behafarid, F.; Cuenya, B. R.; Strasser, P. Particle Size Effects in the Catalytic Electroreduction of CO_2 on Cu Nanoparticles. *J. Am. Chem. Soc.* **2014**, *136*, 6978–6986.

(11) Roberts, F. S.; Kuhl, K. P.; Nilsson, A. High selectivity for ethylene from carbon dioxide reduction over copper nanocube electrocatalysts. *Angew. Chem.* **2015**, *127*, 5268 –5271.

(12) Zhao, Y.; Wang, C.; Wallace, G.G. Tin nanoparticles decorated copper oxide nanowires for selective electrochemical reduction of aqueous CO_2 to CO. *J. Mater. Chem. A* **2016**, *4*, 10710-10726.

(13) Roberts, F. S.; Kuhl, K. P.; Nilsson, A. Electroreduction of Carbon Monoxide Over a Copper Nanocube Catalyst: Surface Structure and pH Dependence on Selectivity. *Chem. Cat. Chem*. **2016**, *8*, 1119–11124.

(14)   Ren, D.; Wong, N. T.; Handoko, A. D.; Huang, Y.; Yeo, B. S. Mechanistic Insights into the Enhanced Activity and Stability of Agglomerated Cu Nanocrystals for the Electrochemical Reduction of Carbon Dioxide to n-Propanol. *J. Phys. Chem. Lett.* **2016**, *7*, 20-24.

(15) Li, C. W.; Kanan, M. W. CO_2 reduction at low overpotential on Cu electrodes resulting from the reduction of thick Cu_2O films. *J. Am. Chem. Soc*. **2012**, *134*, 7231−7234.

(16) Li, C. W.; Ciston, J., Kanan, M. W. Electroreduction of carbon monoxide to liquid fuel on oxide-derived nanocrystalline copper. *Nat. lett.* **2014**, *508*, 504-507.

(17) Kas, R.; Kortlever, R.; Milbrat, A.; Koper, M. T. M.; Mul, G.; Baltrusaitis, J. Electrochemical CO_2 reduction on Cu_2O-derived copper nanoparticles: controlling the catalytic selectivity of hydrocarbons *J. Phys. Chem. Chem. Phys*., **2014**, *16*, 12194-12201.

(18) Lee, S.; Kim, D.; Lee, J. Electrocatalytic Production of C3-C4 Compounds by Conversion of CO_2 on a Chloride-Induced Bi-Phasic Cu_2O-Cu Catalyst. *Angew. Chem.* **2015**, *127*, 14914 – 14918.

(19) Mistry, H.; Varela, A. S.; Bonifacio, C.S.; Zegkinoglou, I.; Sinev, I.; Choi,Y.-W.; Kisslinger, K.; Stach,E.A.; Yang, J.C.; Strasser, P.; Cuenya, B. R. Highly selective plasma-activated copper catalysts for carbon dioxide reduction to ethylene. *Nat. Comm.* **2016**, *7*, 12123-1-8.

(20) Verdaguer-Casadevall, A.; Li, C. W.; Johansson, T. P.; Scott, S. B.; McKeown, J. T.; Kumar, M.; Stephens, I. E. L.; Kanan, M. W.;   Chorkendorf, I. Probing the Active Surface Sites for CO Reduction on Oxide-Derived Copper Electrocatalysts. *J. Am. Chem. Soc.* **2015**, *137*, 9808–9811.

(21) Le, M.; Ren, M.; Zhang, Z.; Sprunger, P. T.; Kurtz, R. L.; Flake, J. C. Electrochemical Reduction of CO_2 to CH_3OH at Copper Oxide Surfaces *J. Electrochem. Soc.,* **2011**, *158*, E45-E49.

(22) Frese, K. W. Electrochemical Reduction of CO_2 at Intentionally Oxidized Copper Electrodes. *J. Electrochem. Soc.,* **1991**, *138,* 3338-3344.

(23) Beverskoga, B.; Puigdomenech, I. Revised Pourbaix Diagrams for Copper at 25 to 300°C *J. Electrochem. Soc.,* **1997**,*144*, 3476-3483.

(24) Eilert, A.; Cavalca, F.; Roberts, F. S.; Osterwalder, J.; Liu, C.; Favaro, M.; Crumlin, E. J.; Ogasawara, H.; Friebel, D.; Pettersson, L. G. M.; Nilsson A. Subsurface Oxygen in Oxide-Derived Copper Electrocatalysts for Carbon Dioxide Reduction *J. Phys. Chem. Lett.* **2017**, *8*, 285−290.

(25) Hong, J., Zhang, W., Ren, J.; Xu, R. Photocatalytic reduction of CO_2: a brief review on product analysis and systematic methods. *Anal. Methods* **2013**, *5,* 1086–1097.

(26) Brown, T.A.; Chen, H.; Zare, R. N.; Identification of Fleeting Electrochemical Reaction Intermediates Using Desorption Electrospray Ionization Mass Spectrometry. *J. Am. Chem. Soc*., **2015**, *137*, 7274–7277.

(27) Adams, N. G.; Smith, D. The selected ion flow tube (SIFT); A technique for studying ion neutral reactions. *Int. J. Mass Spectrom. Ion Phys.,* 1976, *21***,** 349–359.

 (28) Smith, D., Diskin, A. M., Ji, Y. & Španěl, P. Concurrent use of H_3O+, NO+, and O_2+ precursor ions for the detection and quantification of diverse trace gases in the presence of air and breath by selected ion-flow tube mass spectrometry. *Int. J. Mass Spectrom.,* **2001**, *209***,** 81–97 .

(29) Ferguson, E. E. Ion-Molecule Reactions. *Annu. Rev. Phys. Chem.,* **1975**, *26***,** 17–38.

(30) Lobaccaro, P.; Mandal, L.; Motapothula, M. R.; Sherburne, M.; Martin, J.; Venkatesan, T.; Ager, J. W. Initial Application of Selected-Ion Flow-Tube Mass Spectrometry to Real-Time Product Detection in Electrochemical CO2 Reduction *Energy Technol..* **2017**,*5*, 1-13.

(31) Deo, M.; Mujawar, S.;   Game, O.; Yengantiwar, A.; Banpurkar, A.; Kulkarni, S.; Jog, J.; Ogale, S. Strong photo-response in a flip-chip nanowire p-Cu_2O/n-ZnO junction. *Nanoscale*, **2011**, *3*, 4706-4712.

(32) Lobaccaro, P.; Singh, M.; Clark, E. L.; Kwan, Y.; Bell, A.T.; Ager, J.W. Effects of temperature and gas-liquid mass transfer on the operation of small electrochemical cells for the

quantitative evaluation of CO_2 reduction electrocatalysts. *Phys. Chem. Chem. Phys.*, **2016**, *18*, 26777-26785.

(33) Kresse, G.; Hafner, J. Ab initio molecular dynamics for liquid metals. *Phys. Rev. B* **1993,** *47* (1), 558-561.

(34) Kresse, G.; Hafner, J. Ab initio molecular-dynamics simulation of the liquid-metal– amorphous-semiconductor transition in germanium. *Phys. Rev. B* **1994,** *49* (20), 14251-14269.

(35) Kresse, G.; Furthmüller, J. Efficiency of ab-initio total energy calculations for metals and semiconductors using a plane-wave basis set. *Comput. Mater. Sci.* **1996,** *6* (1), 15-50.

(36) Kresse, G.; Furthmüller, J. Efficient iterative schemes for ab initio total-energy calculations using a plane-wave basis set. *Phys. Rev. B* **1996,** *54* (16), 11169-11186.

(37) Blöchl, P. E. Projector augmented-wave method. *Phys. Rev. B* **1994,** *50* (24), 17953-17979.

(38) Kresse, G.; Joubert, D. From ultrasoft pseudopotentials to the projector augmented-wave method. *Phys. Rev. B* **1999,** *59* (3), 1758-1775.

(39) Perdew, J. P.; Burke, K.; Ernzerhof, M. Generalized Gradient Approximation Made Simple. *Phys. Rev. Lett.* **1996,** *77* (18), 3865-3868.

(40). Mills, G.; Jonsson, H.; Schenter, G. K Reversible work transition state theory: application to dissociative adsorption of hydrogen *Surface Science*, **1995,***324*, 305-337.

(41) Heyden, A.; Bell, A. T.; Keil, F. J. Efficient methods for finding transition states in chemical reactions: Comparison of improved dimer method and partitioned rational function optimization method *J. Chem. Phys.* **2005**, *123*, 224101 1-14.

(42) Nørskov, J. K.; Rossmeisl, J.; Logadottir, A.; Lindqvist, L. Origin of the overpotential for oxygen reduction at a fuel-cell cathode. *J. Phys. Chem. B*, **2004**, *108*, 17886–17892.

(43) Grimme, S.; Antony, J.; Ehrlich, S.; Krieg , H. A consistent and accurate ab initio parametrization of density functional dispersion correction „DFT-D… for the 94 elements H-Pu. J. Chem. Phys., **2010**, *132*, 154104 1-19.

(44) K. Mathew, R. Sundararaman, K. Letchworth-Weaver, T. A. Arias, and Richard G. Hennig Implicit solvation model for density-functional study of nanocrystal surfaces and reaction pathways. J. Chem. Phys., **2014**, *140*, 084106 1-9.

(45) Solache-Carranco, H.; Juárez-Díaz, G.; Galván-Arellano, M.; Martínez-Juárez, J. ; Romero-Paredes , G. ; Peña-Sierra, R. Raman scattering and photoluminescence studies on Cu_2O. *IEEE, CCE* **2008,** Catalog Number: CFP08827-CDR.

(46) Lum, Y.; Ager, J. W. Stability of Residual Oxides in Oxide-Derived Cu Catalysts for Electrochemical CO_2 Reduction Investigated with 18O Labeling *Angew. Chem. Int. Ed.* **2018**, *57*,551 –554.

 (47) Ren, X.; Rinke, P.; Scheffler, M. Exploring the random phase approximation: application to CO adsorption. *Phys. Rev. B,* **2009**, *80*, 045402 1-8.

(48) Hori, Y.; Murata, A.; Takahashi, R. Formation of hydrocarbons in the electrochemical reduction of carbon dioxide at a copper electrode in aqueous solution. *J. Chem. Soc., Faraday Trans. 1*, **1989**, *85*, 2309-2326.

(49) Peterson, A. A.; Abild-Pedersen, F.; Studt, F.; Rossmeisl, J.; Nørskov, J. K. How copper catalyzes the electroreduction of carbon dioxide into hydrocarbon fuels. *Energy Environ. Sci.* **2010**, *3*, 1311-1315.

(50) Deng, Y.; Handoko, A. D.; Du, Y.; Xi, S.; Yeo, B.S. In Situ Raman Spectroscopy of Copper and Copper Oxide Surfaces during Electrochemical Oxygen Evolution Reaction: Identification of CuIII Oxides as Catalytically Active Species. *ACS Catal.* **2016**, *6*, 2473−2481.

(51) Akemann, W.; Otto, A. The effect of atomic scale surface disorder on bonding and activation of adsorbates: vibrational properties of CO and CO_2 on copper. *Surf. Sci.* **1993**, *287/288*, 104-109.

(52) Chen, C. Y.; Burstein, E.; Lundquist S. Giant Raman Scattering by Pyridine And CN Adsorbed On Silver. *Sol. State Comn.*, **1979**, *32*, 63-66.

(53) Smith, B.; Irish, D.; Kedzierzawski, P.; Augustynski, J. A Surface Enhanced Raman Scattering Study of the Intermediate and Poisoning Species Formed during the Electrochemical Reduction of CO_2 on Copper. *J. Electrochem. Soc.* **1997**, *144*, 4288−4296.

(54) Frantz, J. D. Raman spectra of potassium carbonate and bicarbonate aqueous fluids at elevated temperatures and pressures: comparison with theoretical simulations. *Chem. Geology,* **1998**, *152*, 211-225.

(55) Dunwell, M.; Lu, Q.; Heyes, J. M.; Rosen, J.; Chen, J. G.; Yan, Y.; Jiao, F.; Xu, B. The Central Role of Bicarbonate in the Electrochemical Reduction of Carbon Dioxide on Gold. *J. Am. Chem. Soc.* **2017**, *139*, 3774−3783.

(56) Heyes, J.; Dunwell, M.; Xu, B.; CO2 Reduction on Cu at Low Overpotentials with Surface-Enhanced in Situ Spectroscopy. *J. Phys. Chem. C*, **2016**, *120*, 17334–17341.

(57)Hori, Y.; Koga, O.; Watanabe, Y.; Matsuo, T.; FTIR measurements of charge displacement adsorption of CO on poly- and single crystal (100) of Cu electrodes. *Electrochimica Acta* **1998**, 44, 1389-1395.

(58) Wuttig, A.; Liu, C.; Peng, Q.; Yaguchi, M.; Hendon, C. H.; Motobayashi, K.; Ye, S.; Osawa, M.; Surendranath, Y. Tracking a Common Surface-Bound Intermediate during CO_2-to-Fuels Catalysis. *ACS Cent. Sci*. **2016**, *2*, 522–528.

(59) Dutta, A.; Kuzume, A.; Rahaman, M.; Vesztergom, S.; Broekmann, P. Monitoring the Chemical State of Catalysts for CO_2 Electroreduction: An In Operando Study. *ACS Catal.* **2015**, *5*, 7498−7502.

(60) Calle-Vallejo, F.; Koper, M. T. M. Theoretical Considerations on the Electroreduction of CO to C2 Species on Cu (100) Electrodes. *Angew. Chem. Int. Ed.* **2013**, *52*, 7282 –7285.

 (61) Hori, Y.; Murata, A.; Tsukamoto, T.; Wakebe, H.; Koga, O.; Yamazaki, H. Adsoprtion of carbon monoxide at a copper electrode accompanied by electron transfer observed by voltammetry and IR spectroscopy. *Electrochim. Acta*, **1994**, *39*, 2495-2648.

(62) Hori, Y.; Wakebe, H.; Tsukamoto, T.; Koga, O. Adsorption of CO accompanied with simultaneous charge transfer on copper single crystal electrodes related with electrochemical reduction of CO_2 to hydrocarbons. *Surf. Sci*. **1995**, *335*, 258-263.

(63) Nie, X.; Esopi, M. R.; Janik, M. J.; Asthagiri, A. Selectivity of CO_2 Reduction on Copper Electrodes: The Role of the Kinetics of Elementary Steps. *Angew. Chem. Int. Ed.* **2013**, *52*, 2459 −2462.

(64) Akhade, S. A.; Luo, W.; Nie, X.; Bernstein, N. J.; Asthagiri, A.; Janik, M. J. Poisoning effect of adsorbed CO during CO_2 electroreduction on late transition metals. *Phys. Chem. Chem. Phys.,* **2014**, *16*, 20429-20435.

(65) Kas, R.; Kortlever, R.; Yılmaz, H.; Koper, M. T. M.; Mul, G. Manipulating the Hydrocarbon Selectivity of Copper Nanoparticles in CO_2 Electroreduction by Process Conditions *ChemElectroChem* **2015**, *2*, 354 − 358.

(66) Eilert, A.; Roberts, F. S.; Friebel, D.; Nilsson A. Formation of Copper Catalysts for CO_2 Reduction with High Ethylene/Methane Product Ratio Investigated with In Situ X-ray Absorption Spectroscopy. *J. Phys. Chem. Lett.,* **2016**, *7*, 1466–1470.

(67) Lum, Y.; Yue, B; Lobaccaro, P.; Bell, A. T.; Ager, J. W. Optimizing C−C Coupling on Oxide-Derived Copper Catalysts for Electrochemical CO2 Reduction J. Phys. Chem. C, 2017, 121, 14191−14203.

(68) Favaro, M.; Xiao, H.; Cheng, T.; Goddard, W. A.; Yano, J.; Crumlin, E. J. Subsurface oxide plays a critical role in CO2 activation by Cu(111) surfaces to form chemisorbed CO2, the first step in reduction of CO2 *Proc. Natl. Acad. Sci.* **2017**, *114*, 6706-6711.

Table of Contents (TOC) Image